Biosensors and Bioelectronics 127 (2019) 92–100

Contents lists available at ScienceDirect

Biosensors and Bioelectronics

journal homepage: www.elsevier.com/locate/bios

Construction of Ce-MOF@COF hybrid nanostructure: Label-free aptasensor for the ultrasensitive detection of oxytetracycline residues in aqueous solution environments

Nan Zhou[a], Yashen Ma[b], Bin Hu[b], Linghao He[b], Shijun Wang[a,*], Zhihong Zhang[b,*], Siyu Lu[c,*]

[a] Department of Orthopedics, The First Affiliated Hospital of Zhengzhou University, No. 1, Jianshe East Road, Zhengzhou 450052, PR China
[b] Henan Provincial Key Laboratory of Surface and Interface Science, Zhengzhou University of Light Industry, No. 136, Science Avenue, Zhengzhou 450001, PR China
[c] College of Chemistry and Molecular Engineering, Zhengzhou University, Zhengzhou 450000, China

ARTICLE INFO

Keywords:
Ce-based metal organic frameworks
Covalent organic frameworks
Detection of oxytetracycline
Aptamer sensor
Electrochemical impedance spectroscopy

ABSTRACT

Porous organic framework (COF) nanomaterials have drawn increasing attention and showed promising potential in the applications of various fields. Nevertheless, its applications in biosensing or biomedical fields are still in the early stage. In this work, we designed and synthesized a series of nanohybrids of COF and Ce-based metal organic framework (Ce-MOF) for the first time as label-free bioplatforms for a sensitive electrochemical aptasensor to detect oxytetracycline (OTC). A novel kinds of Ce-MOF@COF hybrids were prepared by adding different dosages of COF, into the preparation system of Ce-MOF, for which COF was synthesized using melamine and cyanutic acidmonomers through polycondensation (represented by MCA). Basic characterizations revealed that Ce-MOF@MCA nanohybrids not only remained their orignal crystal and chemical structure and features, such as different Ce species containing in Ce-MOF (Ce^{3+} and Ce^{4+}), various functional amino-groups of MCA, and individual frameworks, but also showed a large specific surface area and interpenetrated morphologies. As a result, the Ce-MOF@MCA hybrid with high content of MCA exhibited high bioaffinity toward the OTC-targeted aptamer, further leading to the incremental detection effect for OTC detection. Among different hybrid-based aptasensors, the Ce-MOF@MCA-based one with an MCA dosage of 500 mg exhibited the lowest limit of detection at 17.4 fg mL^{-1} within a wider linearity of the OTC concentration within 0.1–0.5 ng mL^{-1}. Additionally, the fabricated aptasensor displayed excellent analytical performance with great reproducibility, high selectivity and stability, and acceptable applicability for detecting OTC in various aqueous solutions, including milk, wastewater, and urine samples. This new Ce-MOF@MCA hybrid will become an excellent aptasensors platform for detecting various analytes, such as antibiotics, heavy metal ions, or cancer markers, and it have shown the promissing application potentials in the fields of biomedicine, food safety and environmental monitoring.

1. Introduction

Antibiotics have been widely used in treating cow mastitis (Barton, 2000); thus, the consumption of animal products contaminated with antibiotic residues can cause allergic reactions in humans and reduce the efficacy of antibiotics for treating human infections (Huang et al., 2018; Mishra et al., 2018; Rodríguez et al., 2009). Among the commercially available tetracyclines, oxytetracycline (OTC) is the most commonly used tetracycline in food-producing animals due to the approval of the European Union and the United States Food and Drug Administration for therapeutic use (Kim et al., 2014). However, the conventional techniques often require high-cost instrumentation, extensive and time-consuming sample-processing, and skilled technicians in a laboratory (Singh et al., 2018; Talan et al., 2018). Therefore, it is extremely necessary to develop a simple, highly sensitive and selective methods for detecting OTC in the biological fluids. To date, aptamers have been widely considered as the main specific oligonucleotides (single strand DNA or RNA) for capturing and detecting various targets which are obtained through in vitro selection, also referred to as systematic evolution of ligands by exponential enrichment (SELEX) (Aswani Kumar et al., 2018; Jayasena, 1999). Compared with antibodies, aptamers are easily synthesized, modified and fixed, repeatedly used, and preserved for long term (Niazi et al., 2008). Since Niazi et al. selected a DNA aptamer which could be used to specifically

* Corresponding authors.
E-mail addresses: fccwangsj3@zzu.edu.cn (S. Wang), 2006015@zzuli.edu.cn (Z. Zhang), sylu2013@zzu.edu.cn (S. Lu).

https://doi.org/10.1016/j.bios.2018.12.024

Available online 18 December 2018

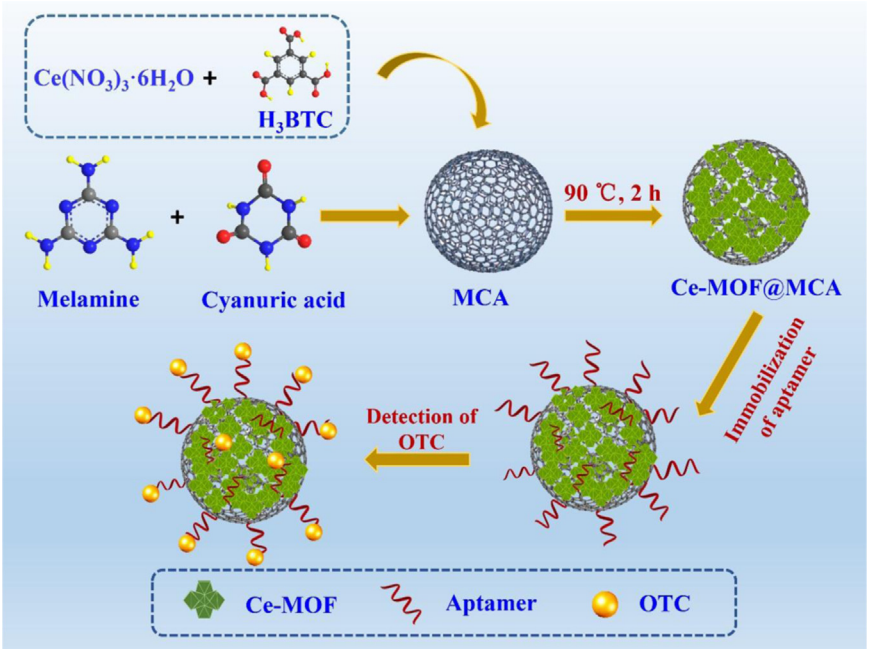

Scheme 1. Schematic diagram of the fabrication procedure of the Ce-MOF@MCA-based aptasensor for detecting OTC, including (i) the preparation of the series of Ce-MOF@MCA hybrids, (ii) the immobilization of the aptamer strands over the Ce-MOF@MCA hybrid, and (iii) the OTC detection using the proposed Ce-MOF@MCA-based aptasensor.

detect OTC in 2008 (Cháfer-Pericás et al., 2010), numerous studies had developed an aptamer-based biosensor for OTC analysis in the applications of food safety and environmental monitoring based on fluoroimmunoassay (Kim et al., 2010), colorimetric (C. Liu et al., 2017; S. Liu et al., 2017), electrochemical (Kim and Lee, 2017), and surface plasmon resonance methods (Yang et al., 2015). Among them, electrochemical aptasensors could provide easy, highly sensitive, cost-effective, and sensitive detection without requirement of high-cost equipments (Li et al., 1999). To obtain aptasensors with high sensitivity and selectivity, enhancing the compatibility between biomolecules and electrochemistry is important. The use of solid electrodes with specific nanostructures containing electroactive labels have opened a new area in biomolecule detection (Hui and Ying, 2017).

Metal-organic frameworks (MOFs), a promising class of multifunctional materials, have received extensive attention since 1999 (Falcaro et al., 2014). Their tunable structures, large surface areas, and high thermal and chemical stabilities allow their wide application in gas storage and separation, catalysis, drug delivery, and biosensing (Guo et al., 2017). Additionally, the strong electrostatic, π-π stacking, and/or hydrogen-bonding interactions between oligonucleotide strands and MOFs allow immobilization of aptamer strands over various MOFs (G. Chen et al., 2017; M. Chen et al., 2017; He and Duan, 2017). Consequently, a large number of MOFs have been employed as platforms for DNA or aptamer biosensors for sensitively detecting antibiotics (Chen et al., 2016; Wang et al., 2018). UiO-66-NH_2 (Zr-MOF)-based electrochemical aptasensor was developed for simultaneous detection of OTC and kanamycin (Kana), showing limits of detection (LODs) of 0.18 and 0.15 pM, respectively (Zhang et al., 2017a, 2017b). In our previous work, a series of Zr-MOFs composites embedded with three kinds of aptamer strands were achieved by a one-step de novo synthetic approach and exploited as platforms for the ultrasensitive detection of various analytes, including thrombin, kanamycin (Kana), and carcinoembryonic antigen (C. Liu et al., 2017; S. Liu et al., 2017). The developed Al-MOF-based electrochemical biosensor was used to detect vomitoxin and salbutamol, giving low LODs of 0.70 and 0.40 pg mL^{-1}, respectively (Xiong et al., 2015). Cerium-based MOF exhibits intrinsic oxidase-like activity, showing excellent mimics of catalytic activity toward 3,3′,5,5′-tetramethylbenzidine (Shi et al., 2017). Furthermore, Ce-MOF-based aptasensor was developed to detect adenosine triphosphate (Shen et al., 2016) and Zn^{2+} (Zhang et al., 2017a, 2017b). Nevertheless, most MOFs have low electrochemical activity. Usually, MOFs are often combined with other nanomaterials to improve their electrochemical signals when used as electrochemical biosensing platforms, such as metal nanoclusters (Liu et al., 2016), quantum dots (Jin et al., 2017), and metal oxides (Côté et al., 2005; Falcaro et al., 2016).

Similarly, covalent organic frameworks (COFs) are a class of novel crystalline porous polymer with well-defined structural regularity, large surface area, and tunable pore structure that have attracted increasing attention since 2005 (Segura et al., 2016). The tunable channel allows the wide application of COFs in heterogeneous catalysis (Olivos-Suarez et al., 2016), gas storage and adsorption (Du et al., 2015), pH or chemical sensing (Li et al., 2016), proton conduction (Xu et al., 2016), and energy storage (Ding et al., 2016). To date, Wang's (Dalapati et al., 2016) and Jiang's group (Peng et al., 2017) have applied COFs in the field of sensing. However, it exhibited the limited selectivity due to lacking of a specific recognition group (H. Wang et al., 2017; Y. Wang et al., 2017). Therefore, a sensitive and selective COF-based turn-on sensor is highly desirable. When immobilizing probe molecules (DNA or aptamer strands) through π-π stacking and hydrogen-bonding interaction, COFs can also act as the biosensing scaffold for the targeted detection of analytes (Fu et al., 2016). The exploration of new porous hybrid materials is still important because of their unique properties and promising applications in the separation of materials and catalysis (Schwarz et al., 2001). However, there are few reports about the applications of COFs or COF-on-MOF integration in electrochemical biosensing, especially in food safety testing.

Based the above analysis, we synthesized a novel kinds of Ce-MOF and COF nanohybrids, where COF was synthesized through the reaction of melamine and cyanuric acid (represented by MCA). The obtained Ce-MOF and MCA nanohybrid (denoted by Ce-MOF@MCA) was exploited as a scaffold of the OTC aptasensor for the first time (Scheme 1). Considering the excellent biosensing performances of Ce-MOF (Yang et al., 2015), the electrochemical activity originated from the porous carbon support and high surface area of MCA (Guo et al., 2016) and the high sensitivity and selectivity of the electrochemical aptasensors, the as-obtained Ce-MOF@MCA-based aptasensor exhibits an extremely low LOD toward OTC in comparison with the individual Ce-MOF- and MCA-based aptasensors. Also, the proposed aptasensor shows highly selectivity, good stability and reproducibility, and excellent applicability

in aqueous solution environments. As compared with the platform materials of routine OTC aptasensors, the Ce-MOF@MCA hybrid displays three outstanding advantages, including the following points: (i) strong interaction between aptamer strands and the Ce-MOF@MCA, such as strong electrostatic, π-π stacking, and/or hydrogen-bonding interactions, can strength the aptamer immobilization and OTC adsorption (Yang et al., 2013); (ii) the instinct cavities within the MOF and COF frameworks can not only facilitate aptamer strands to immobilize over the substrate surface but also can impel them to penetration into the pore channels, further resulting in large amounts of aptamer strands binding and OTC detection (Dogru et al., 2013); and (iii) combining highly conjugated structure of MCA and electrochemical activity of Ce-MOF can endow the proposed hybrid with high electrochemical signal. The present work can provide a potential method to develop novel electrochemical MOFs@COF-based aptasensors and broaden their applications in food safety, biomedical, and biosensing fields.

2. Experimental section

The detailed description of materials and reagents, pre-treatment of the bare Au electrode (AE), characterizations, and electrochemical measurements were supplied in S1 (See the Supplementary material).

2.1. Synthesis of MCA, Ce-MOF nanorod, and series of Ce-MOF@MCA nanohybrids

The synthesis of MCA nanosheets was referred to the reported literature (Guo et al., 2016). In brief, equal molar amounts of melamine (0.50 g) and cyanuric acid (0.51 g) were first dissolved in 20 and 10 mL dimethyl sulfoxide to form the transparent solution, respectively. The solutions of melamine and cyanuric acid were then mixed together under the vigorous stirring. After reaction for 30 min, the white precipitate was washed with ethanol repeatedly for three times and then dried at 60 ˚C in the oven to obtain MCA supramolecular aggregates.

Ce-MOF was obtained according to the literature (G. Chen et al., 2017; M. Chen et al., 2017). Typically, 434 mg $Ce(NO_3)_3{\cdot}6H_2O$ was solved in an ethanol/water solution (40 mL, $v{:}v$ = 1:1) under vigorous stirring and ultrasonication at room temperature to form the homogeneous suspension. 1,3,5-benzenetricarboxylic acid (H_3BTC) (210 mg) was dissolved in an ethanol/water (v/v = 1/1, 10 mL) mixture to can form a clear solution. The H_3BTC solution was added in the $Ce(NO_3)_3{\cdot}6H_2O$ solution, and the reaction mixture was then refluxed at 90 ˚C for 2 h. After cooling to room temperature naturally, the white precipitate was collected by centrifugation and washed with an equal amount of ethanol/water mixture several times, and then dried in an oven at 60 ˚C. As such, Ce-MOF was obtained.

For the Ce-MOF@MCA_{100} nanohybrid preparation, 100 mg MCA was added in the preparation system of Ce-MOF. Concurrently, Ce-MOF@MCA_{300} and Ce-MOF@MCA_{500} nanohybrids were synthesized by using the same method when using the dosage of 300 and 500 mg, accordingly.

2.2. Preparation of phosphate buffered saline, aptamer, OTC, and real sample solutions

Phosphate buffer solution (PBS, pH 7.4, 0.1 M) was prepared by KH_2PO_4, Na_2HPO_4, NaCl and KCl. PBS containing 5 mM $[Fe(CN)_6]^{3-/4-}$ was employed as a redox probe for cyclic voltammetry (CV) and electrochemical impedance spectroscopy (EIS) characterizations. The stock aptamer solution (100 nM) and different concentration of OTC solutions were prepared with 0.1 M PBS. All solutions were prepared immediately prepared before each experiment and stored at 4 ˚C until use.

The liquid milk was purchased from the local supermarket and pretreated according to the general procedure (Zhang et al., 2013). First, 5 mL of trichloroacetic acid (60 mM) and 35 mL of methanol solution (5 M) were added to 500 mL of milk to eliminate proteins and extract analyte. Subsequently, the mixture was centrifuged at 10,000 rpm for 10 min after sonicating 15 min and shaking for 10 min. Then, the supernatant was filtrated through a 0.45 μm microporous membrane to get the milk sample. Moreover, the river water was obtained from Xushui River (Henan province, China) was filtered through a microporous membrane (0.22 μm) and then centrifuged at 10,000 rpm for 30 min. The urine was obtained from adult male and filtered through a microporous membrane (0.22 μm) to be the real sample. The known amounts of antibiotics were dissolved into the sample to acquire different concentrations of antibiotics solutions for further analysis.

2.3. Fabrication of the aptasensor

As for the fabrication of the Ce-MOF@MCA_{100}-based aptasensor, 1.0 mg prepared Ce-MOF@MCA_{100} powder was dispersed in 1.0 mL of deionized water, followed by ultrasonic agitated for 30 min to form a homogeneous suspension liquid with the concentration of 1.0 mg mL^{-1}. The Ce-MOF@MCA_{100} suspension (5.0 μL, 1.0 mg mL^{-1}) was dropped to the surface of the pre-treated AE and dried in ambient air for 1 h. The resultant modified electrode was represented by the Ce-MOF@MCA_{100}/AE. Afterward, the Ce-MOF@MCA_{100}/AE was immersed into the OTC-targeted aptamer solution (100 nM) for 30 min and washed with excess of PBS (pH 7.4) thoroughly to remove unbound aptamer strands. The obtained electrochemical aptasensor was represented by Apt/Ce-MOF@MCA_{100}/AE and applied to detect OTC (1.0 $pg{\cdot}mL^{-1}$). Simultaneously, the MCA-, Ce-MOF-, Ce-MOF@MCA_{300}-, and Ce-MOF@MCA_{500}-based aptasensors were prepared in the same manner.

3. Results and discussion

3.1. Sensing mechanism

A series of novel Ce-MOF@MCA hybrids was synthesized by preparing Ce-MOF with different amounts of MCA. Owning to the high specific area, rich chemical functionality, and excellent electrochemical activity, many aptamer strands can not only anchor over the Ce-MOF@MCA surface but can also penetrate into the interior of porous Ce-MOF@MCA networks by π-π stacking interaction and strong electrostatic interaction between the aptamer strands and the organic frameworks (Scheme 1) (Peng et al., 2016; Schwarz et al., 2001). As a result, the OTC-targeted aptamer immobilized over Ce-MOF@MCA networks can supply amide bonds for a target-specific moiety with OTC, further forming a G-quadruplex structure between the OTC and the aptamer strands (Tan et al., 2016). When adding the OTC solution, the aroused conformational change will induce a steric hindrance, which prevents redox probes from accessing the AE surface and further decrease the electrochemical activity (Radi et al., 2009).

3.2. Chemical structures and components

The crystal and chemical structures of all samples were characterized by X-ray diffraction and Fourier transform infrared spectroscopy (Fig. S1) (See S1 of the Supplementary material). XPS characterizations were performed to further investigate the chemical components. The main element signals (Fig. S4) and atomic contents (%) of each element (Table S1) were analyzed and shown in **S1**. To evaluate chemical variations before and after combining Ce-MOF and different dosages of MCA, the Ce 3*d*, C 1s, N 1s, and O 1 *s* core-level XPS spectra were analyzed using the PEAKXPS1 software. The core-level XPS spectra of each element containing MCA were analyzed (See S1, Fig. S5), in which the presence of N=C−N and N−C=O indicates the formation of MCA through Schiff-base condensation at a solid-vapor interface (Nasab et al., 2018). Furthermore, the π-π* conjugated framework of MCA can enhance the electrochemical activity.

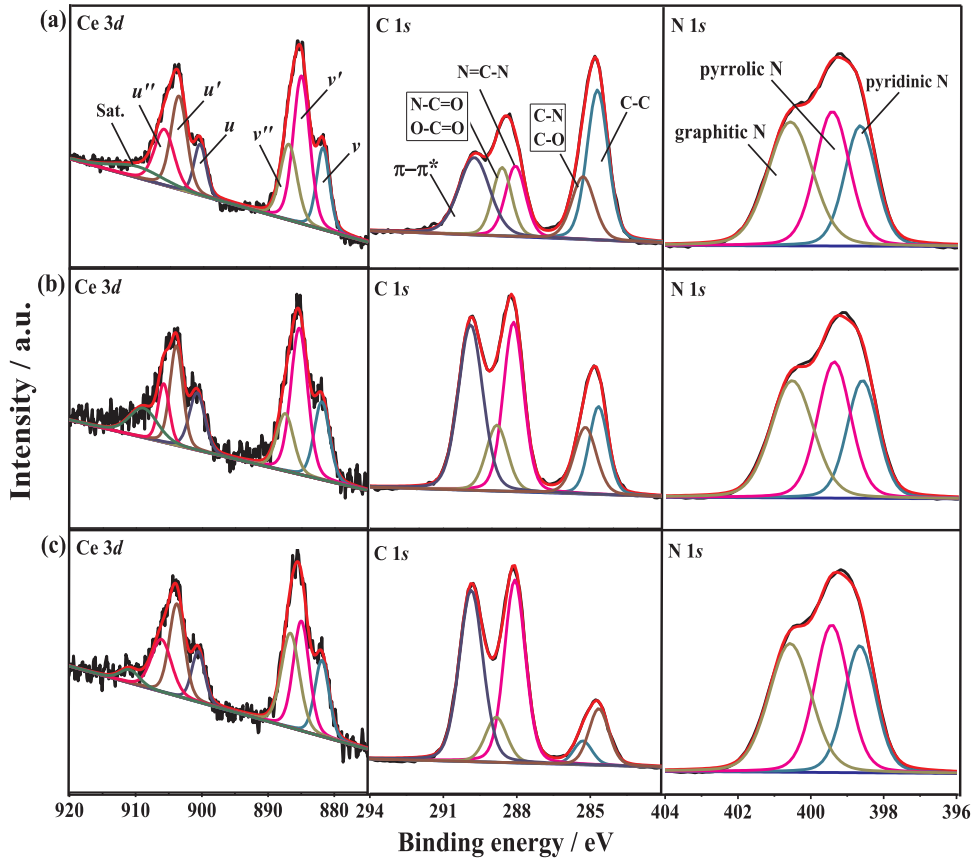

Fig. 1. Ce 3*d*, C 1*s* and N 1*s* core-level XPS spectra of (a) Ce-MOF@MCA_{100}, (b) Ce-MOF@MCA_{300} and (c) Ce-MOF@MCA_{500} nanohybrids.

The Ce 3*d*, C 1*s*, and O 1*s* core-level XPS spectra of Ce-MOF were also fitted (Fig. S6). It shows the Ce 3*d* XPS spectrum was formed by two multiplets (*v* and *u*), which were assigned to the spin-orbit split $3d_{5/2}$ and $3d_{3/2}$ core holes (Fig. S6a), respectively (G. Chen et al., 2017; M. Chen et al., 2017). Four peaks of *u*″ (906.1 eV), *u* (900.3 eV), *v*″ (887.1 eV), and *v* (881.6 eV) were argued to be characteristics of Ce^{4+}, whereas the two peaks of *u*′ (903.6 eV) and *v*′ (885.0 eV) were attributed to Ce^{3+} (Mukherjee et al., 2016). The satellite peak at 910.7 eV was due to the characteristic signature of Ce^{4+}. Consequently, Ce-MOF is composed of a mixed valence-state metal center of Ce^{4+} and Ce^{3+}. The C 1*s* core-level XPS spectrum was deconvoluted into four components (Fig. S6b) at 284.7, 285.7, 288.4, and 290.6 eV, corresponding to C—C, C—O, C=O, and π-π*bonding moieties, respectively. It is clear for that all fitted C 1 s peaks were attributed to the used organic ligands. For the O 1*s* core-level XPS spectrum of Ce-MOF, an additional peak at 530.8 eV was obtained, which was attributed to the Ce—O bonds compared with MCA.

Concurrently, the Ce 3*d*, C 1*s*, N 1*s*, and O 1*s* core-level XPS spectra of the series of Ce-MOF@MCA were also analyzed and summarized in Fig. 1 and S7. Owing to the combination of MCA with Ce-MOF, the contents of Ce 3*d* signals are lower than that of the pristine Ce-MOF. Fig. 1**a** shows the same deconvolution of the obtained Ce 3*d* as that of Ce-MOF. Moreover, the fitted C 1*s* core-level XPS spectra of Ce-MOF@MCA hybrids are composed of MCA and Ce-MOF. The intensity of C—C group decreases, whereas those of N—C=N and π-π groups increase with increasing MCA dosage, consistent with the experimental condition. Also, the presence of π-π conjugated structure is favorable to immobilize the DNA strands and enhance the stability of the fabricated sensors (Kim and Lee, 2017). No substantial change in N 1*s* (Fig. 1) and O 1*s* (Fig. S7) deconvolution spectra were observed after the hybridization of MCA and Ce-MOF compared with those of MCA.

3.3. Surface morphologies of the series of Ce-MOF@MCA nanohybrids

The surface morphologies of MCA, Ce-MOF, and the series of Ce-MOF@MCA hybrids were characterized by SEM and TEM. As shown in the part of **S2,** MCA illustrates porous sphere-like morphology in the SEM images (Figs. S8a and S8b), which is confirmed by its TEM images (Figs. S8c and S8d). Its sphere-like nanostructure is aggregated by multilayered nanosheets with many pores, hinting the porous nanostructure of MCA spheres. The HRTEM image of MCA shows that it is composed of nanosheets with the amorphous structure (Fig. S8d). From Figs. S9a and S9b, the prepared Ce-MOF exhibits an aligned firewood structure. Due to the aggregated interaction, Ce-MOF nanorods are easily integrated into large bunches. The TEM image of Ce-MOF (Fig. S9c) reveals that the size of Ce-MOF nanorods is not uniform. It also reveals their amorphous structure due to the absence of clear lattice spacing (Fig. S9d).

The morphologies of the series of Ce-MOF@MCA nanohybrids are displayed in Fig. 2. Combined with 100 mg MCA (Fig. 2**a** and **b**), the nanorod length of the synthesized Ce-MOF@MCA_{100} becomes shorter but with a larger diameter comparing with Ce-MOF nanorods. The TEM image of Ce-MOF@MCA_{100} demonstrates that the Ce-MOF nanorods only mix with the MCA nanosheets due to the small usage of MCA. With increased dosage of MCA to 300 mg (Fig. 2**d** and **e**), the Ce-MOF@MCA_{300} nanohybrid is composed of many nanorods with irregular shape. It means that the addition of MCA affects the formation mechanism of Ce-MOF. The TEM image of Ce-MOF@MCA_{300} nanohybrid (Fig. 2**f**) displays that short Ce-MOF nanorods are embedded within the MCA nanosheets. With increased dosage of MCA nanosheets to 500 mg, i.e., Ce-MOF@MCA_{500} nanohybrid, Ce-MOF nanorods are wrapped with the MCA layer, indicating the successful combination of Ce-MOF and MCA.

Additionally, the N_2 adsorption–desorption isotherms of MCA, Ce-

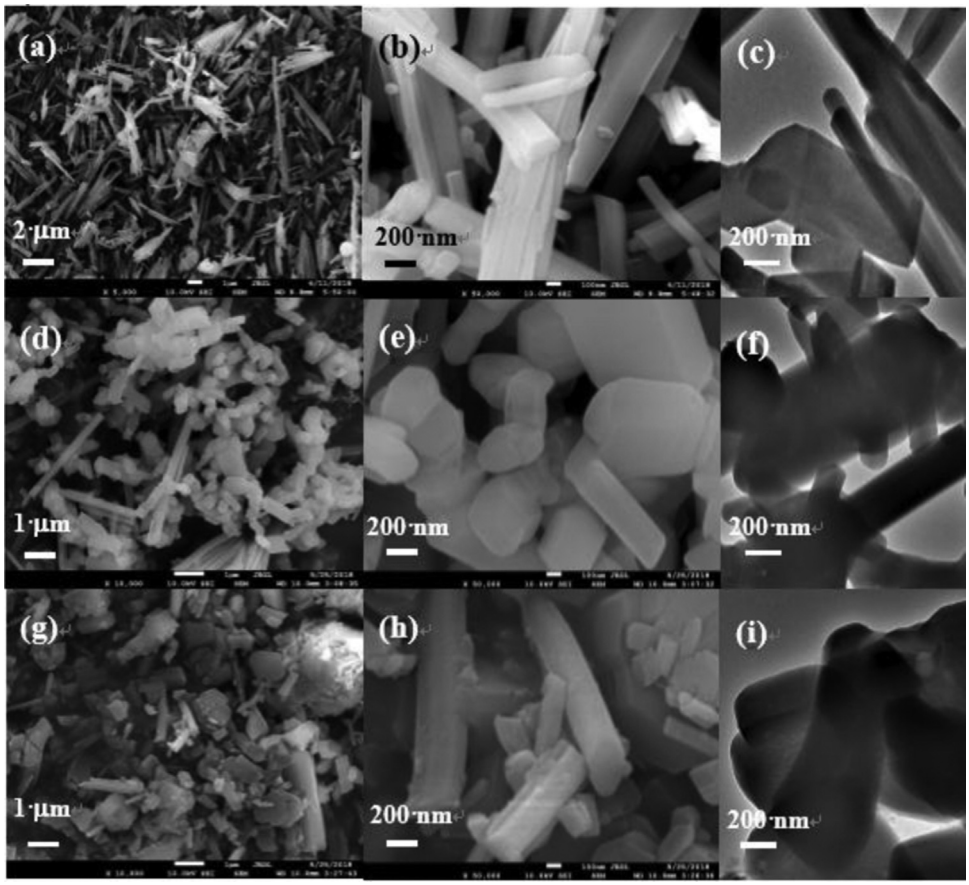

Fig. 2. SEM and TEM images of (a, b, c) Ce-MOF@MCA_{100}, (d, e, f) Ce-MOF@MCA_{300} and (g, h, i) Ce-MOF@MCA_{500} nanohybrids.

MOF nanorod, and the series of Ce-MOF@MCA nanohybrids were measured, as displayed in Fig. S10, where the specific surface areas of MCA and Ce-MOF are 16.56 and 4.72 $m^2\ g^{-1}$, respectively. After combining Ce-MOF with different dosages of MCA, the specific areas of Ce-MOF@MCA_{100}, Ce-MOF@MCA_{300}, and Ce-MOF@MCA_{500} nanohybrids are 9.10, 36.67, and 46.72 $m^2\ g^{-1}$, respectively. It demonstrates that the specific surface area of Ce-MOF@MCA_{500} is the largest among three nanohybrids, which is favorable to the aptamer strand immobilization (Wang et al., 2016).

3.4. Electrochemical sensing performances of all samples

EIS techniques can effectively supply impedance change information during the surface modification of the electrode (Li et al., 2011). EIS diagrams are simulated using the Randles equivalent circuit consisting of solution resistance (R_s), charge-transfer resistance (R_{ct}), constant-phase element, and the Warburg impedance (W) (the inset of Fig. S11a). Herein, the EIS measurements of the whole procedure for detecting OTC based on the proposed aptasensors for the five samples (MCA, Ce-MOF, and the series of Ce-MOF@MCA) were simultaneously carried out, including the modification step of AE with the nanomaterials, the immobilization of aptamer strands, and the OTC detection (Figs. S11 and 3**a**). The simulated R_{ct} values of AE at different steps for the five samples are summarized in Table S2. It demonstrates similar trends for the different sensing systems. The AE modification of the five samples increases the R_{ct} value, which is ascribed to the relatively poor electrochemical activity of the ALD layers. Also, the immobilization of the aptamer strands over the modified layers increases R_{ct} due to electrostatic repulsion between the negatively charged deoxyribose-phosphate backbone of the OTC-targeted aptamer strands and $[Fe(CN)_6]^{3-/4-}$ anions (G. Zhang et al., 2015; H. Zhang et al. 2015). It confirms the successful immobilization of aptamer to form the sensing interface. When the aptasensor was exposed to OTC, the R_{ct} value continuously increases. This observation can be attributed to the conformational changes of the anti-OTC aptamers upon specific binding to OTC, which further prevent the electron transfer at the interface (Qiao et al., 2018). In order to optimize the sensing conditions for detecting OTC, the factors, including the Ce-MOF@MCA_{500} coverage onto the electrode surface (Fig. S12), the aptamer concentration (Fig. S13), the incubation time of aptamer strands (Fig. S14a and S14b), and the binding time of OTC (Fig. S14c and S14d), were considered and used to investigate their influence on detecting OTC. The experiment results and detailed description were supplied in S5 (See the Supplementary material). It demonstrates that the optimal sensing parameters for the Ce-MOF@MCA_{500}-based aptasensor are shown as followed: the usage of Ce-MOF@MCA_{500} is 1.0 mg mL^{-1}; the aptamer concentration is 100 nM; the incubation time of aptamer is 30 min; and the binding time of OTC is 60 min.

Since the R_{ct} value can represent the adsorbed amount of the anchored layer (Sheikhzadeh et al., 2016), R_{ct} variations caused by aptamer strand immobilization and OTC detection correspond to the anchoring ability toward aptamer and OTC detection sensitivity, respectively. Although OTC determination by using different aptasensors has similar trends, the difference in R_{ct} ($\Delta R_{ct} = R_{ct,i+1} - R_{ct,1}$) caused by different sensing systems at each step are varying, as illustrated in Fig. 3**b**. Among five different samples, the ΔR_{ct} value caused by the MCA layer is the smallest at 0.036 kΩ, suggesting its excellent electrochemical activity, which originated from the conjugated structure of MCA (Salunkhe et al., 2018). Conversely, the ΔR_{ct} value obtained from the Ce-MOF is the largest at 0.891 kΩ. It hints that the presence of Ce-MOF prevents the electron from transferring at the interface between Ce-MOF and electrolytes, due to the semi-conductivity

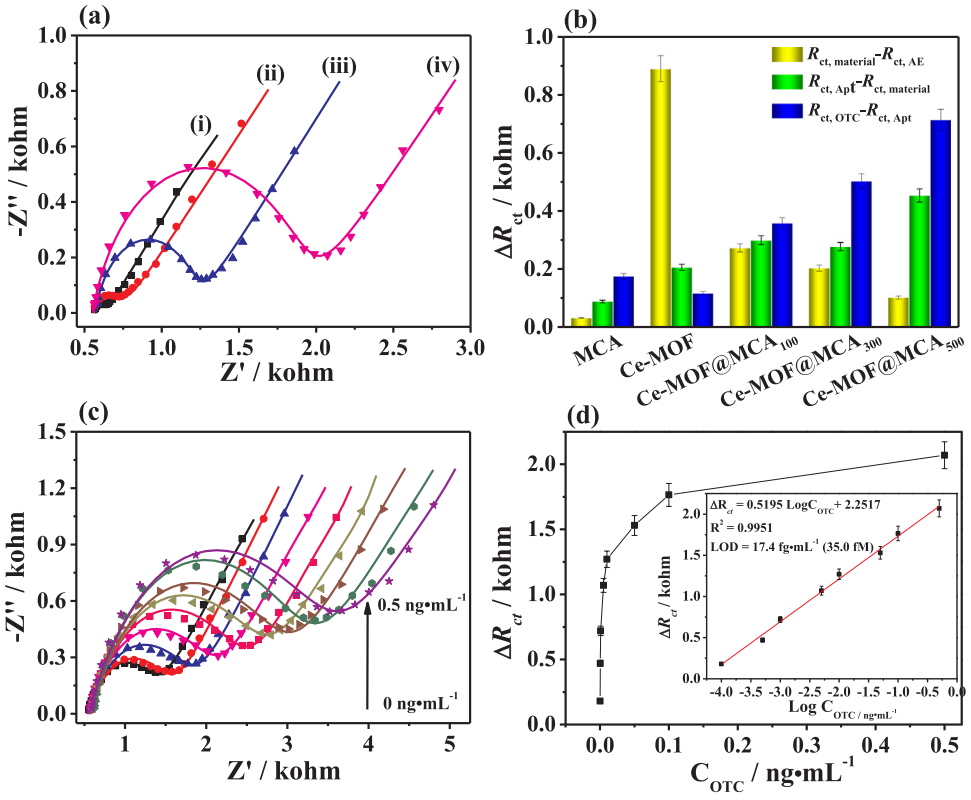

Fig. 3. (a) EIS Nyquist plots of the OTC detection procedures using the electrochemical aptasensors based on Ce-MOF@MCA$_{500}$ in 5 mM $[Fe(CN)_6]^{3-/4-}$ containing 0.1 M KCl, including (i) AE, (ii) AE/Ce-MOF@MCA$_{500}$, (iii) AE/Ce-MOF@MCA$_{500}$/Apt, and (iv) AE/Ce-MOF@MCA$_{500}$/Apt/OTC. (b) The corresponding variations of the R_{ct} values of the five kinds of aptasensors for detecting OTC detection procedures (n = 3). (c) EIS Nyquist plots for the detection of different concentrations of OTC (0.0001, 0.0005, 0.001, 0.005, 0.01, 0.05, 0.1, and 0.5 ng mL^{-1}) using the Ce-MOF@MCA$_{500}$-based aptasensor. (d) The corresponding calibration curves between ΔR_{ct} and OTC concentrations (Inset: the linear fit plot of ΔR_{ct} as function of the logarithm of OTC concentration (n = 3)).

Table 1
Comparison of the proposed method for OTC biosensors with other previously reported works.

Materials	Detection method	Linear range (nM)	LOD (nM)	Ref.
GO-Adenosine hydrogel	Fluorescent assay	50–2 × 10^3	50	(W. Li et al., 2017; Y. Li et al., 2017)
RhB-modified Au NPs	Spectrofluorimetry	2.0–1 × 10^3	0.32	(Abolhasani and Farajzadeh, 2014)
ITO/TiO_2/H-DNA@QD	Photoelectrochemical	2–300	0.19	(W. Li et al., 2017; Y. Li et al., 2017)
aptamer-templated AgNPs	Fluorescence quenching	0.50–100	0.10	(Hosseini et al., 2016)
$NaYF_4$:$Y_{b,Tm}$ upconversion nanoparticles	Luminescence resonance energy transfer	0.217–21.72	0.117	(G. Zhang et al., 2015; H. Zhang et al. 2015)
MWCNTs/HRP	Electrocatalytic oxidation	3 × 10^{-3}–34	0.27	(Ghodsi et al., 2016)
Fe_3O_4 MNPs	Aptamer-based fluorescence	2.2–109	1.80	(Liu et al., 2015)
Aptamer probes	Microchip electrophoresis	2 × 10^{-3}–2.0	1.81 pM	(H. Wang et al., 2017; Y. Wang et al., 2017)
GR-3D Au film	Differential pulse voltammetry (DPV)	1.09 × 10^{-3}– 4.34 × 10^3	1.08 pM	(Peng et al., 2017)
Ce-MOF@MCA$_{500}$	Electrochemical impedance spectroscopy	2 × 10^{-4}–1.0	35.0 fM	This work

and poor electrochemical activity of MOFs (Qi et al., 2018). Additionally, the ΔR_{ct} value caused by the aptamer strand immobilization of Ce-MOF is higher than that of MCA layer, indicating that more aptamer strands can adsorb onto the Ce-MOF framework with high specific surface area and Ce-O coordination centers (Zheng et al., 2014). However, the ΔR_{ct} for the combination of aptamer strands and OTC for Ce-MOF is less than that of MCA. It indicates the poor interaction between the formed G-quadruplex and Ce-MOF, further causing the release of G-quadruplex from the substrate. Thereby, the MCA layer can not only strengthen the electrochemical activity but can also stabilize the G-quadruplex of aptamer strands and OTC molecules in aqueous solution. As expected, with increased MCA dosage from 100 to 500 mg, the ΔR_{ct} for the modification of these hybrids decreases from 0.277 to 0.105 kΩ, whereas the ΔR_{ct} values for OTC detection increases from 0.361 to 0.715 kΩ. Consequently, the Ce-MOF@MCA$_{500}$ hybrid exhibits the highest immobilization amount of aptamer, further leading to the highest detection sensitivity toward OTC. Due to the excellent electrochemical activity and strong stabilization of the formed G-quadruplex when detecting OTC, the Ce-MOF@MCA$_{500}$-based aptasensor was selected for further electrochemical measurements.

3.5. Detection sensitivity of the Ce-MOF@MCA$_{500}$-based aptasensor toward OTC

The sensitivity of the developed Ce-MOF@MCA$_{500}$-based aptasensors was evaluated by measuring the dependence of ΔR_{ct} on OTC concentrations (Con$_{OTC}$). The corresponding EIS Nyquist plots are illustrated in Fig. 3**c**, showing that the obtained R_{ct} values increase with increasing the OTC concentration and hinting that more OTC molecules can be recognized by the aptamer strands. The relationship between ΔR_{ct} and Con$_{OTC}$ is presented in Fig. 3**d**, where ΔR_{ct} substantially increases with increasing Con$_{OTC}$ within 0.1–0.5 ng mL^{-1} for OTC. At an OTC concentration above 0.01 ng mL^{-1}, it increases slowly. From the inset of Fig. 3**d**, a linear relationship is observed between ΔR_{ct} and the logarithm of Con$_{OTC}$ within 0.1–0.5 ng mL^{-1}. The regression equation was ΔR_{ct} (kΩ) = 0.5195 log Con$_{OCT}$ + 2.2517 (Con$_{OTC}$: ng mL^{-1}) with a regression coefficient (R^2) of 0.9951. The LOD for OTC was 17.4 fg mL^{-1} (S/N = 3). As compared with the reported aptasensors (Table 1), Ce-MOF@MCA$_{500}$-based ones have a lower LOD and better detection performances, which displays superior biosensing performance of the fabricated aptasensor. It is mainly due to the following reasons: (i) the high specific surface area of Ce-MOF@MCA caused by its regular

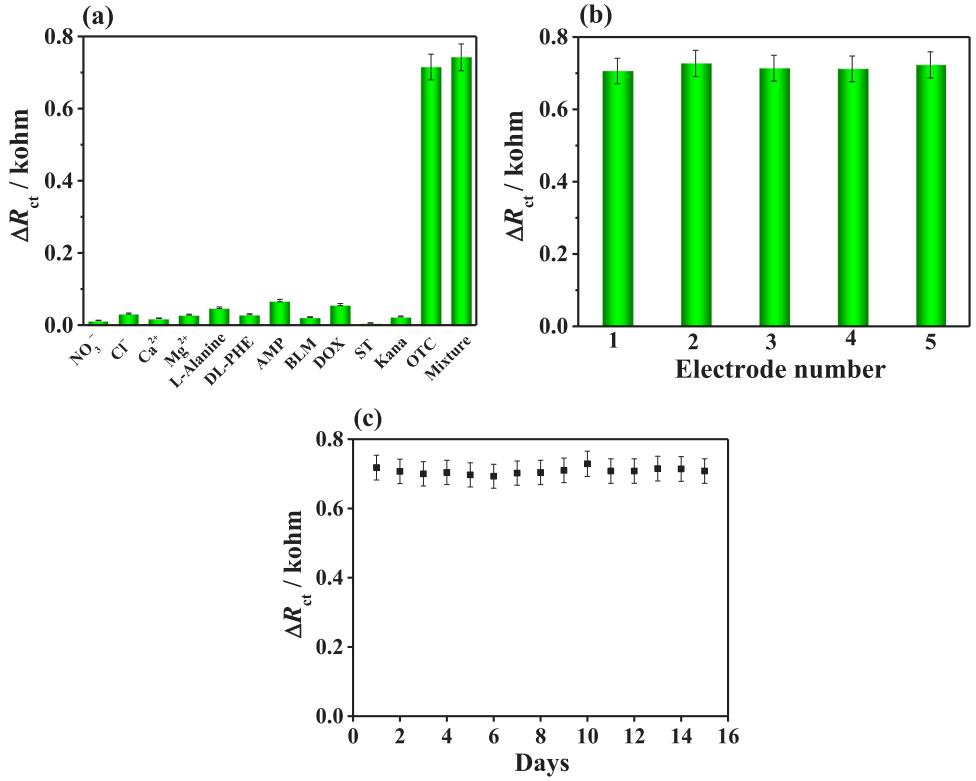

Fig. 4. (a) The selectivity, (b) reproducibility, and (c) stability of the Ce-MOF@MCA_{500}-based aptasensor for detection of 1.0 pg mL^{-1} OTC (n = 3).

frameworks and porous nanostructure not only can facilitate the adsorption of small molecules but also can increase the anchored amounts of aptamer strands (Jia et al., 2016); (ii) the coexistence of the Ce-MOF@COF frameworks and the highly conjugated degree of MCA can strengthen the stability of the aptamer strands after the recognition of analyte molecules through hydrogen bonding, π-π stacking and electrostatic interactions (Kim and Lee, 2017; Yang et al., 2015) that further improve the aptasensor stability and reproducibility; and (iii) the excellent electrochemical activity of MCA heightens the sensing performances of the proposed aptasensor (Díaz and Corma, 2016).

3.6. Selectivity, stability, and reproducibility of the Ce-MOF@MCA_{500}-based aptasensors

To evaluate selectivity of the proposed aptasensor, the influences of some ions, biomolecules, and other antibiotics were studied. A substantial signal of 1.0 pg mL^{-1} OTC was observed, whereas electrochemical signals caused by interferents are negligible (Fig. 4**a**), including NO_3^-, Cl^-, Ca^{2+}, Mg^{2+}, L-Alanine, DL-Phenylalanine (DL-PHE), AMP (Ampicillin), BLM (Bleomycin), doxycycline hyclate (DOX), streptomycin sulphate (ST), kanamycin (Kana), uric acid (UA), and urea with 100-folds of the OTC concentration. The mixture of OTC with interferents was also investigated, which has a comparable signal with OTC. It indicates that interferents can not affect the OTC detection. These findings confirm the excellent selectivity of the proposed aptasensor.

To access the reproducibility of the fabricated electrochemical aptasensor, five electrodes modified with Ce-MOF@MCA_{500} were simultaneously prepared, following the same aptamer immobilization and OTC detection procedure. Fig. 4**b** displays comparable ΔR_{ct} values for the OTC detection of each biosensing system. It shows that a relative standard deviation (RSD) toward OTC (1.0 pg mL^{-1}) of around 1.16%, suggesting the good reproducibility of the developed aptasensor. Meanwhile, the used Ce-MOF@MCA_{500}-based aptasensor was stored in the refrigerator at 4 °C and measured daily. The signal barely changed after 15 days toward OTC (1.0 pg mL^{-1}), suggesting its high stability (Fig. 4**c**).

3.7. Real sample analysis

To further investigate the feasibility of the proposed aptasensor, we used it to detect OTC in various aqueous solutions, including milk, wastewater, and urine. Different OTC solution with various concentrations were spiked separately into the treated milk, wastewater and urine, followed by the determination by using the Ce-MOF@MCA_{500}-based aptasensor through the aforementioned EIS method. According to the mentioned linear equation, the obtained OTC levels are shown in Table 2, yielding recoveries of 101.9–113.6%, 94–103.7%, and 92.6–106.5% in milk, river water, and urine, respectively. It displays that all RSD values are less than 5%. Therefore, the proposed Ce-MOF@MCA_{500}-aptasensor not only exhibits good reproducibility and accuracy but also shows excellent feasibility for the rapid OTC detection in the analysis of real samples.

4. Conclusions

In summary, we synthesized a series of novel nanostructured Ce-MOF@MCA hybrids with different amounts of MCA layers embedded within Ce-MOF for the first time. The obtained Ce-MOF@MCA hybrids exhibited good stability and excellent dispersion ability in aqueous solution, excellent electrochemical activity, and strong bio-affinity toward aptamer strands. As a result, a series of Ce-MOF@MCA hybrids were used as the scaffold support for immobilizing the OTC-targeted aptamer, further employing to detect trace OTC through EIS technique. By comparing different OTC aptasensors based on Ce-MOF@MCA hybrids which contained various amounts of MCA, the Ce-MOF@MCA_{500}-based aptasensor exhibits high sensitivity, giving an ultra-low LOD of 17.4 fg mL^{-1} with high selectivity, good stability and reproducibility, and an acceptable applicability for detecting OTC. Although the used Ce-MOF@MCA platform includes multiple stages, the present work can

Table 2
Detection of OTC in milk and river water using the developed Ce-MOF@MCA_{500}-based aptasensor (n = 3).

Samples	Added amount (pg mL^{-1})	ΔR_{ct} (kΩ)	Found amount (pg mL^{-1})	Recovery (%)	RSD (%)
Milk	0.1	0.185	0.105	105	1.38
	0.5	0.55	0.53	106	1.31
	1	0.722	1.136	113.6	1.04
	5	1.08	5.55	111	1.02
	10	1.24	11.28	112.8	1.87
	50	1.58	50.94	101.9	2.39
	100	1.76	113.11	113.1	2.06
River water	0.1	0.170	0.098	98	1.53
	0.5	0.522	0.47	94	2.08
	1	0.686	0.969	96.9	1.15
	5	1.045	4.76	95.2	2.65
	10	1.22	10.37	103.7	1.73
	50	1.57	48.51	97.02	2.52
	100	1.727	97.72	97.72	1.57
Urine	0.1	0.172	0.099	99	2.06
	0.5	0.530	0.485	97	1.89
	1	0.702	1.039	103.9	1.47
	5	1.039	4.63	92.6	2.03
	10	1.20	9.45	94.5	1.67
	50	1.59	53.24	106.5	1.89

provide new insight into porous organic frameworks-based aptasensors for detecting trace amounts of harmful small aminoglycosides and exploiting their applications in food safety and environmental monitoring.

Acknowledgements

This work was supported by Programs for the National Natural Science Foundation of China (NSFC: Account Nos. 81601082, 81371363, 81771329 and U1604127) and Innovative Technology Team of Henan Province, China (CXTD2014042).

Conflict of interest statement

We declare that we have no financial and personal relationships with other people or organizations that can inappropriately influence our work, there is no professional or other personal interest of any nature or kind in any product, service and/or company that could be construed as influencing the position presented in, or the review of, the manuscript entitled "*Construction of Ce-MOF@COF hybrid nanostructure: Label-free aptasensor for ultrasensitively detecting oxytetracycline residue in various aqueous environments*".

Appendix A. Supplementary material

Supplementary data associated with this article can be found in the online version at doi:10.1016/j.bios.2018.12.024.

References

Abolhasani, J., Farajzadeh, N., 2014. Luminescence 30, 257–262.
Aswani Kumar, Y.V.V., Renuka, R.M., Achuth, J., Venkataramana, M., Ushakiranmayi, M., Sudhakar, P., 2018. Front. Pharmacol. 9, 271.
Barton, M.D., 2000. Nutr. Res. Rev. 13, 279–299.
Cháfer-Pericás, C., Maquieira, Á., Puchades, R., Miralles, J., Moreno, A., Pastor-Navarro, N., Espinós, F., 2010. Anal. Chim. Acta 662, 177–185.
Chen, G., Guo, Z., Zhao, W., Gao, D., Li, C., Ye, C., Sun, G., 2017a. ACS Appl. Mater. Interfaces 9, 39594–39601.
Chen, M., Gan, N., Zhou, Y., Li, T., Xu, Q., Cao, Y., Chen, Y., 2016. Talanta 161, 867–874.
Chen, M., Gan, N., Zhou, Y., Li, T., Xu, Q., Cao, Y., Chen, Y., 2017b. Sens. Actuators B-Chem. 242, 1201–1209.
Côté, A.P., Benin, A.I., Ockwig, N.W., O., Keeffe, M., Matzger, A.J., Yaghi, O.M., 2005. Science 310, 1166.
Dalapati, S., Gu, C., Jiang, D., 2016. Small 12, 6513–6527.
Ding, S., Dong, M., Wang, Y., Chen, Y., Wang, H., Su, C., Wang, W., 2016. J. Am. Chem. Soc. 138, 3031–3037.
Díaz, U., Corma, A., 2016. Coord. Chem. Rev. 311, 85–124.
Dogru, M., Handloser, M., Auras, F., Kunz, T., Medina, D., Hartschuh, A., Knochel, P., Bein, T., 2013. Angew. Chem. 125, 2992–2996.
Du, Y., Yang, H., Whiteley, J.M., Wan, S., Jin, Y., Lee, S., Zhang, W., 2015. Angew. Chem. Int. Ed. 55, 1737–1741.
Falcaro, P., Ricco, R., Doherty, C.M., Liang, K., Hill, A.J., Styles, M.J., 2014. Chem. Soc. Rev. 43, 5513–5560.
Falcaro, P., Ricco, R., Yazdi, A., Imaz, I., Furukawa, S., Maspoch, D., Ameloot, R., Evans, J.D., Doonan, C.J., 2016. Coord. Chem. Rev. 307, 237–254.
Fu, J., Das, S., Xing, G., Ben, T., Valtchev, V., Qiu, S., 2016. J. Am. Chem. Soc. 138, 7673–7680.
Ghodsi, J., Rafati, A.A., Shoja, Y., 2016. Sens. Actuators B-Chem. 224, 692–699.
Guo, C., Su, F., Song, Y., Hu, B., Wang, M., He, L., Peng, D., Zhang, Z., 2017. ACS Appl. Mater. Interfaces 9, 41188–41199.
Guo, Y., Li, J., Yuan, Y., Li, L., Zhang, M., Zhou, C., Lin, Z., 2016. Angew. Chem. Int. Ed. 55, 14693–14697.
Hosseini, M., Mehrabi, F., Ganjali, M.R., Norouzi, P., 2016. Luminescence 31, 1339–1343.
Huang, Q., Li, X., Feng, S., Zhuge, W., Liu, F., Peng, J., Mo, S., 2018. Anal. Methods 10, 3594–3601.
Hui, G., Ying, Y., 2017. Trans. ASABE 60, 1439–1443.
Jayasena, S.D., 1999. Clin. Chem. 45, 1628.
Jia, X., Dong, S., Wang, E., 2016. Biosens. Bioelectron. 76, 80–90.
Jin, M., Mou, Z., Zhang, R., Liang, S., Zhang, Z., 2017. Biosens. Bioelectron. 91, 162–168.
Kim, C., Lee, L., Min, J., Lim, M., Jeong, S., 2014. Biosens. Bioelectron. 51, 426–430.
Kim, S., Lee, H.J., 2017. Anal. Chem. 89, 6624–6630.
Kim, Y.S., Kim, J.H., Kim, I.A., Lee, S.J., Jurng, J., Gu, M.B., 2010. Biosens. Bioelectron. 26, 1644–1649.
Li, F., Han, X., Liu, S., 2011. Biosens. Bioelectron. 26, 2619–2625.
Li, H., Eddaoudi, M., O'Keeffe, M., Yaghi, O.M., 1999. Nature 402, 276.
Li, W., Yang, C., Yan, X., 2017a. Chem. Commun. 53, 11469–11471.
Li, Y., Tian, J., Yuan, T., Wang, P., Lu, J., 2017. Sens. Actuators B-Chem. 240, 785–792.
Li, Z., Zhang, Y., Xia, H., Mu, Y., Liu, X., 2016. Chem. Commun. 52, 6613–6616.
He, L., Duan, F., 2017. 2D Mater. 4, 25098.
Liu, C., Lu, C., Tang, Z., Chen, X., Wang, G., Sun, F., 2015. Microchim. Acta 182, 2567–2575.
Liu, C., Sun, C., Tian, J., Wang, Z., Ji, H., Song, Y., Zhang, S., Zhang, Z., He, L., Du, M., 2017a. Biosens. Bioelectron. 91, 804–810.
Liu, L., Song, Y., Chong, H., Yang, S., Xiang, J., Jin, S., Kang, X., Zhang, J., Yu, H., Zhu, M., 2016. Nanoscale 8, 1407–1412.
Liu, S., Wang, Y., Xu, W., Leng, X., Wang, H., Guo, Y., Huang, J., 2017b. Biosens. Bioelectron. 88, 181–187.
Mishra, P., Banga, I., Tyagi, R., Munjal, T., Goel, A., Capalash, N., Sharma, P., Suri, C.R., Gandhi, S., 2018. RSC Adv. 8, 23163–23170.
Mukherjee, D., Rao, B.G., Reddy, B.M., 2016. Appl. Catal. B-Environ. 197, 105–115.
Nasab, R.R., Mansourian, M., Hassanzadeh, F., 2018. Res. Pharm. Sci. 13, 213–221.
Niazi, J.H., Lee, S.J., Gu, M.B., 2008. Bioorgan. Med. Chem. 16, 7245–7253.
Olivos-Suarez, A.I., Szécsényi, À., Hensen, E.J.M., Ruiz-Martinez, J., Pidko, E.A., Gascon, J., 2016. ACS Catal. 6, 2965–2981.
Peng, Y., Huang, Y., Zhu, Y., Chen, B., Wang, L., Lai, Z., Zhang, Z., Zhao, M., Tan, C., Yang, N., Shao, F., Han, Y., Zhang, H., 2017. J. Am. Chem. Soc. 139, 8698–8704.
Peng, Y., Wong, W.K., Hu, Z., Cheng, Y., Yuan, D., Khan, S.A., Zhao, D., 2016. Chem. Mater. 28, 5095–5101.
Qi, K., Hou, R., Zaman, S., Qiu, Y., Xia, B.Y., Duan, H., 2018. ACS Appl. Mater. Interfaces 10, 18021–18028.
Qiao, X., Li, K., Xu, J., Cheng, N., Sheng, Q., Cao, W., Yue, T., Zheng, J., 2018. Biosens. Bioelectron. 113, 142–147.
Radi, A., Muñoz-Berbel, X., Lates, V., Marty, J., 2009. Biosens. Bioelectron. 24, 1888–1892.
Rodríguez, N., Ortiz, M.C., Sarabia, L.A., 2009. Anal. Chim. Acta 651, 149–158.
Salunkhe, P.H., Patil, Y.S., Patil, V.B., Navale, Y.H., Dhole, I.A., Ubale, V.P., Maldar, N.N., Ghanwat, A.A., 2018. J. Polym. Res. 25, 147.
Schwarz, S., Kehrenberg, C., Walsh, T.R., 2001. Int. J. Antimicrob. Agent 17, 431–437.
Segura, J.L., Mancheno, M.J., Zamora, F., 2016. Chem. Soc. Rev. 45, 5635–5671.
Sheikhzadeh, E., Chamsaz, M., Turner, A.P.F., Jager, E.W.H., Beni, V., 2016. Biosens. Bioelectron. 80, 194–200.
Shen, W., Zhuo, Y., Chai, Y., Yuan, R., 2016. Biosens. Bioelectron. 83, 287–292.
Shi, P., Zhang, Y., Yu, Z., Zhang, S., 2017. Sci. Rep. 7, 6500.
Singh, S., Mishra, P., Banga, I., S., Parmar, A., Prakash Tripathi, P., Gandhi, S., 2018. BioImpacts 8, 53–58.
Talan, A., Mishra, A., Eremin, S.A., Narang, J., Kumar, A., Gandhi, S., 2018. Biosens. Bioelectron. 105, 14–21.
Tan, B., Zhao, H., Du, L., Gan, X., Quan, X., 2016. Biosens. Bioelectron. 83, 267–273.
Wang, H., Jiao, F., Gao, F., Huang, J., Zhao, Y., Shen, Y., Zhang, Y., Qian, X., 2017a. J. Mater. Chem. B 5, 4052–4059.
Wang, Y., Gan, N., Zhou, Y., Li, T., Hu, F., Cao, Y., Chen, Y., 2017b. Biosens. Bioelectron. 97, 100–106.
Wang, Z., Liu, T., Asif, M., Yu, Y., Wang, W., Wang, H., Xiao, F., Liu, H., 2018. ACS Appl. Mater. Interfaces 10, 27936–27946.
Wang, Z., Yu, J., Gui, R., Jin, H., Xia, Y., 2016. Biosens. Bioelectron. 79, 136–149.
Xiong, Y., Chen, S., Ye, F., Su, L., Zhang, C., Shen, S., Zhao, S., 2015. Chem. Commun. 51, 4635–4638.
Xu, H., Tao, S., Jiang, D., 2016. Nat. Mater. 15, 722.
Yang, J., Wang, Z., Hu, K., Li, Y., Feng, J., Shi, J., Gu, J., 2015. ACS Appl. Mater. Interfaces 7, 11956–11964.
Yang, Y., Asiri, A.M., Tang, Z., Du, D., Lin, Y., 2013. Mater. Today 16, 365–373.

Zhang, G., Deng, S., Cai, W., Cosnier, S., Zhang, X., Shan, D., 2015a. Anal. Chem. 87, 9093–9100.
Zhang, H., Fang, C., Wu, S., Duan, N., Wang, Z., 2015b. Anal. Biochem. 489, 44–49.
Zhang, X., Zhang, Y., Zhao, H., He, Y., Li, X., Yuan, Z., 2013. Anal. Chim. Acta 778, 63–69.
Zhang, Z., Duan, F., Tian, J., He, J., Yang, L., Zhao, H., Zhang, S., Liu, C., He, L., Chen, M., Chen, D., Du, M., 2017a. ACS Sens. 2, 982–989.
Zhang, Z., Ji, H., Song, Y., Zhang, S., Wang, M., Jia, C., Tian, J., He, L., Zhang, X., Liu, C., 2017b. Biosens. Bioelectron. 94, 358–364.
Zheng, Y., Jiao, Y., Zhu, Y., Li, L.H., Han, Y., Chen, Y., Du, A., Jaroniec, M., Qiao, S.Z., 2014. Nat. Commun. 5, 3783.